Manipulating efficient light emission in two-dimensional perovskite crystals by pressure-induced anisotropic deformation

Liu, Sheng; Sun, Shishuai; Gan, Chee Kwan; Fang, Yanan; Xing, Jun; Li, Hongguo; Huang, Wei; Xiong, Qihua; Del Águila, Andrés Granados; Do, Thi Thu Ha; White, Timothy John

2019

Liu, S., Sun, S., Gan, C. K., Del Águila, A. G., Fang, Y., Xing, J., . . . Xiong, Q. (2019). Manipulating efficient light emission in two-dimensional perovskite crystals by pressure-induced anisotropic deformation. Science Advances, 5(7), eaav9445-. doi:10.1126/sciadv.aav9445

https://hdl.handle.net/10356/103662

https://doi.org/10.1126/sciadv.aav9445

OPTICS

Manipulating efficient light emission in two-dimensional perovskite crystals by pressure-induced anisotropic deformation

Sheng Liu[1,2]*, Shishuai Sun[1]*†, Chee Kwan Gan[3]†, Andrés Granados del Águila[2], Yanan Fang[4], Jun Xing[2], T. Thu Ha Do[2], Timothy J. White[4], Hongguo Li[1], Wei Huang[5], Qihua Xiong[2,6,7]†

The hybrid nature and soft lattice of organolead halide perovskites render their structural changes and optical properties susceptible to external driving forces such as temperature and pressure, remarkably different from conventional semiconductors. Here, we investigate the pressure-induced optical response of a typical two-dimensional perovskite crystal, phenylethylamine lead iodide. At a moderate pressure within 3.5 GPa, its photoluminescence red-shifts continuously, exhibiting an ultrabroad energy tunability range up to 320 meV in the visible spectrum, with quantum yield remaining nearly constant. First-principles calculations suggest that an out-of-plane quasi-uniaxial compression occurs under a hydrostatic pressure, while the energy is absorbed by the reversible and elastic tilting of the benzene rings within the long-chain ligands. This anisotropic structural deformation effectively modulates the quantum confinement effect by 250 meV via barrier height lowering. The broad tunability within a relatively low pressure range will expand optoelectronic applications to a new paradigm with pressure as a tuning knob.

INTRODUCTION

Organolead halide perovskites, $MAPbX_3$ (MA, methylammonium; X = Cl, Br, and I), have received great attention in the past few years, stimulated by promising applications such as solar cells (*1*–*4*), as well as nanolasers (*5*–*8*). It is agreed that these perovskites have low defect density, giant oscillator strength, and long carrier diffusion (*6*, *9*). Another great advantage is its facile synthesis due to relatively low crystal formation temperature. High-quality crystal can be grown by both chemical vapor deposition and the solution-based saturation-precipitation method (*10*–*12*). In addition, the halogen composition can be conveniently tuned to achieve tunable wavelength emission (*7*, *8*, *11*). However, the instability in ambient environment still largely limits the performance of related photovoltaic or light-emitting devices (*13*–*15*). Recently two-dimensional (2D) organic-inorganic Ruddlesden-Popper perovskites that have layered structure are emerging as promising candidates for future nanophotonics and optoelectronics (*16*–*18*). Compared to the 3D counterparts, 2D perovskite has enhanced stability, stronger quantum confinement, and greater wavelength tunability (*16*).

Because of their organic-inorganic hybrid nature, organolead halide perovskites have different configurations of organic and inorganic parts, which establish the diversity of the material family. For instance, in 2D perovskite $(PEA)_2PbX_4$, the long-chain phenylethylamine (PEA) molecules spatially separate the inorganic layers, making a multiple quantum well structure. However, in 3D cases such as $MAPbX_3$ and $FAPbX_3$, smaller molecules (methylammonium and formamidinium) occupy vacancies among the octaheral $[PbX_3]^-$ frame. When hydrostatic pressure is applied to organolead halide perovskites, both components contribute to the lattice structure change, leading to complicated structures and properties. For $MAPbX_3$ under high pressure, similar phenomena are observed from its bulk crystal (*19*–*22*) and nanocrystals (*23*–*25*), including bandgap narrowing, multiple phase transitions with bandgap "blue jump" at different pressures (*20*, *23*), and metalization at ultrahigh pressure up to 50 GPa (*21*). The photoluminescence (PL) of $MAPbX_3$ quenches rapidly and disappears at ~1.5 GPa, making the effective bandgap tunability with efficient PL very limited, generally less than 80 meV (*20*, *23*, *25*). The effective bandgap tunability of $FAPbX_3$ can be 40 meV greater (*26*, *27*) but still insufficient for tunable optoelectronic applications. The rapid quench of PL is attributed to lattice distortion and bending of chemical bonds (*20*–*22*, *26*, *27*). Molecular size and configuration play a key role in controlling the lattice and band structures of organolead halide perovskite under pressure.

2D perovskite with its unique multiple quantum well structure has inherent 2D crystal nature and out-of-plane quantum and dielectric confinements, making a novel platform to realize unique structure and optical properties under pressure. Recently more prominent band tunability with anisotropic compression of lattice has been reported on 2D perovskite (*28*–*30*). Here, we loaded 2D perovskite $(PEA)_2PbI_4$ into a diamond anvil cell (DAC) and systematically studied its optical and structural behaviors under pressure, using steady-state and time-resolved PL (trPL), Raman spectroscopy, x-ray diffraction (XRD) with a synchrotron radiation, and first-principles calculation. Ultrabroad tunable emission has been observed, starting from 2.38 eV (0 GPa) and reaching full quenching at 1.84 eV (~6.2 GPa). The 320-meV tunability at 0 to 3.5 GPa is fully reversible and immediately responds to pressure changes, without a noticeable drop of emission intensity. This tunable high-efficiency emission is device friendly, as the performing pressure is relatively low and achievable without the need of DAC. For

[1]School of Science, Tianjin University of Technology, Tianjin 300384, China. [2]Division of Physics and Applied Physics, School of Physical and Mathematical Sciences, Nanyang Technological University, Singapore 637371, Singapore. [3]Institute of High Performance Computing, 1 Fusionopolis Way, 16-16 Connexis, Singapore 138632, Singapore. [4]School of Materials Science and Engineering, Nanyang Technological University, Singapore 639798, Singapore. [5]Shaanxi Institute of Flexible Electronics (SIFE), Northwestern Polytechnical University (NPU), 127 West Youyi Road, Xi'an 710072, China. [6]MajuLab, CNRS-UNS-NUS-NTU International Joint Research Unit, UMI 3654, Singapore 639798, Singapore. [7]NOVITAS, Nanoelectronics Center of Excellence, School of Electrical and Electronic Engineering, Nanyang Technological University, Singapore 639798, Singapore.
*These authors contributed equally to this work.
†Corresponding author. Email: qihua@ntu.edu.sg (Q.X.); sssdashuai@email.tjut.edu.cn (S.S.); ganck@ihpc.a-star.edu.sg (C.K.G.)

potential applications as tunable lasing, we have found evidence to show that the optical quality regarding the exciton radiative recombination rate is enhanced by pressure within the optical reversible region. The mechanism of the efficient light emission during the bandgap narrowing is well explained by analyzing the structure evolution based on XRD and first-principles calculation. As a result, strong anisotropic deformation of 2D perovskite crystal preserves the lattice structure and the $[PbI_6]^{4-}$ octahedral geometry, thus sustaining the efficiency of band-edge exciton recombination. The prominent thickness reduction of the organic barrier layers releases the quantum confinement and contributes the most to the bandgap red shift of the reversible region.

RESULTS

We sealed 2D perovskite microplates [$(PEA)_2PbI_4$] with a ~40-μm in-plane size and a thickness of ~1 μm in symmetric DAC to perform in situ hydrostatic pressure study, as illustrated in Fig. 1A. We exfoliated the microplates from high-quality single crystal with highly oriented layer structure (see fig. S2). Ruby spheres with a diameter of ~12 μm were put in the chamber for pressure calibration (see fig. S1) (*31*, *32*). By applying pressure, the fluorescence of the nanostructure gradually changes from green to red. A series of fluorescent microscopic images are taken from the investigated $(PEA)_2PbI_4$ crystal sheet inside the DAC (Fig. 1B) at the same lamp power. Within 3.5 GPa, the fluorescence can recover to its original color if the pressure is gradually released. However, after 3.5 GPa, the fluorescence quenches rapidly and loses the reversibility. The process of the fluorescence quenching is shown by the images labeled overloading. While the fluorescence of $(PEA)_2PbI_4$ is weaker, the fluorescence of ruby sphere becomes more visible. These observations suggest that the structural change and fluorescence tunability of $(PEA)_2PbI_4$ are reversible at a modest pressure within 3.5 GPa and irreversible at higher pressures.

Pressure-dependent PL, trPL, and Raman spectra

We investigated the hydrostatic pressure–induced changes of $(PEA)_2PbI_4$ using in situ PL, trPL and Raman spectroscopy at room temperature (Fig. 2). All the PL spectra in Fig. 2A are obtained under the same conditions, showing the evolution with varying pressure. At the beginning, the spectral peak position of PL shifts to lower energy as pressure increases, maintaining a constant intensity level. The peak position can recover its original energy when the pressure is released before 3.5 GPa. After 3.5 GPa, the PL intensity drops markedly and cannot recover by decompression. The result is consistent with the fluorescent images, which together determine the reversible region (within 3.5 GPa) and irreversible region (beyond 3.5 GPa) in the compression process of $(PEA)_2PbI_4$ under hydrostatic pressure. In the reversible region, the energy position of PL varies from green (2.38 eV) to red (2.06 eV), indicating large tunability across the visible spectrum. Although the PL intensity quenches in the irreversible region, the peak position keeps evolving toward lower energy until the PL fully disappears. The last several spectra beyond 4.5 GPa (Fig. 2B) show split peaks, which is likely due to the degeneracy of the excitonic levels lift by pressure. Previous low-temperature absorption and PL measurements have demonstrated multiple excitonic levels in organolead halide perovskites (*33*–*35*), and those levels can be affected by temperature and crystal lattice structure.

Figure 2C shows nonresonant Raman spectra taken under different pressures. To avoid resonance excitation with the tunable PL, we alternatively used 1.96- and 2.33-eV laser lines. Vibration modes at low wave number are prominent in the spectra. All the modes notably blue-shift with increasing pressure. Low–wave number Raman modes less than 50 cm^{-1} were commonly used to determine molecular interactions and orientation of benzene rings (*36*–*38*). Here, the low–wave number vibration modes can describe the interactions between the adjacent benzene rings located at different layers of $(PEA)_2PbI_4$. The strong blue shift suggests that the intermolecular (interlayer) vibration frequency increases distinctly. Apparently, the interlayer

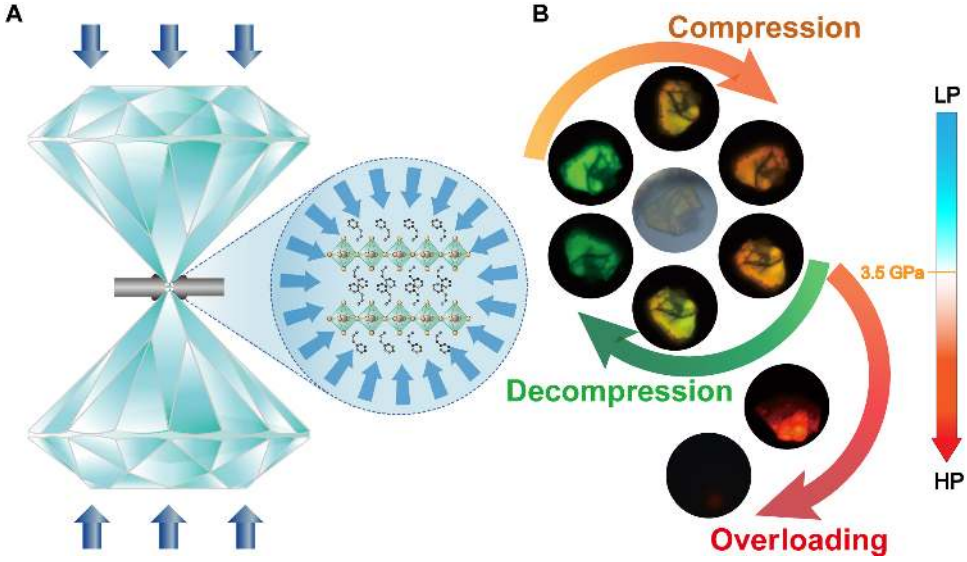

Fig. 1. Schematics of the experiment and optical emission behavior of the 2D perovskite $(PEA)_2PbI_4$ under high pressure. (**A**) Illustration of DAC and the mechanism of hydrostatic compression. (**B**) A set of fluorescent microscopic images of a $(PEA)_2PbI_4$ crystal taken at the same lamp power. A bright-field image of the sample is presented in the center, surrounded by fluorescent images corresponding to different pressures. At 0 to 3.5 GPa, the fluorescence of $(PEA)_2PbI_4$ is equally bright, and the color is reversible by decompression. After 3.5 GPa, the fluorescence rapidly disappears and loses the reversibility. LP, low pressure; HP, high pressure.

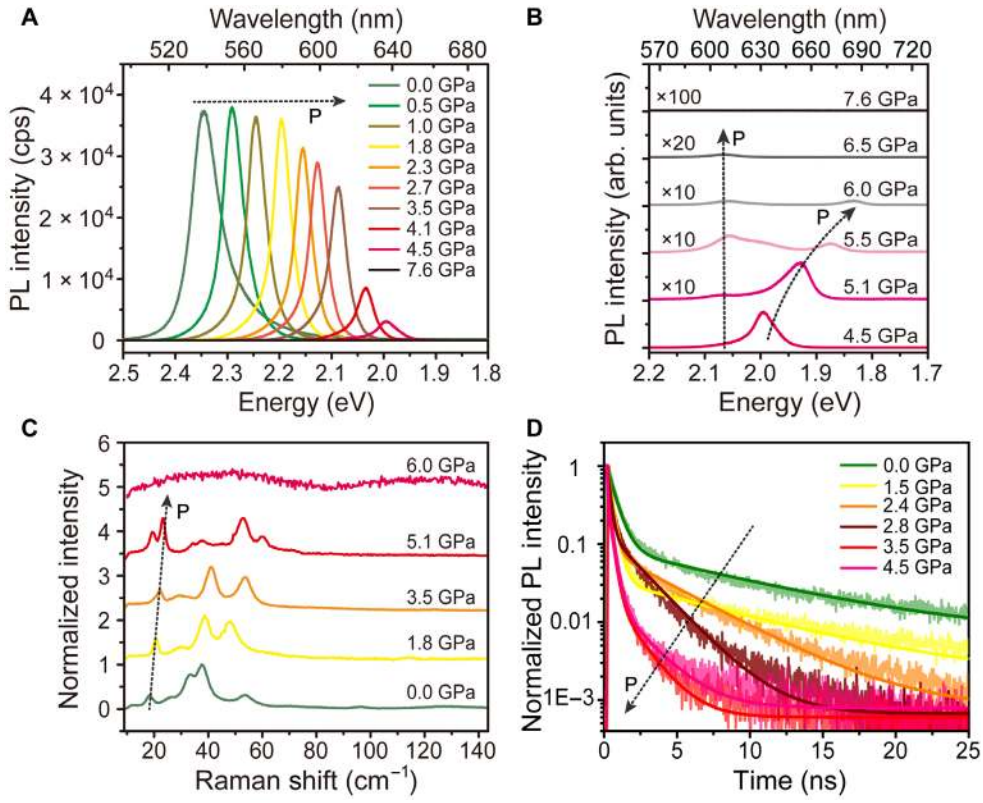

Fig. 2. Spectroscopic measurements of 2D perovskite $(PEA)_2PbI_4$ under high pressure. The dotted arrows in all panels point to the direction of increasing pressure. (**A**) PL spectra excited by 2.62-eV (473-nm) blue laser. The last few spectra when pressure exceeds 4.5 GPa look flat due to low intensity. Intensity axis shows real counts per second (cps) as excitation power is fixed. (**B**) Zoom-in of PL spectra at pressure ranging from 4.5 to 7.6 GPa. arb. units, arbitrary units. (**C**) Raman spectra excited by 1.96-eV (633-nm) laser (when emission is green) and 2.33-eV (532-nm) laser (when emission is red). (**D**) trPL spectra. The smooth lines are biexponential decay fittings of the raw decay data.

interaction is enhanced, which is likely due to the reduction of interlayer distance during compression process. The shift of Raman modes is reversible at moderate pressure range (shown in fig. S6), which is in excellent agreement with the reversible region determined by PL measurements. It is notable that a split of Raman peaks is observed at 5.1 GPa, similar to the PL spectra at the same pressure. When the pressure reaches up to 6 GPa, the Raman modes and the PL vanish synchronously.

Figure 2D shows the trPL spectra as a function of pressure. Those spectra exhibit apparent biexponential decay with fast and slow components, which are related to the two robust room-temperature excitons (see fig. S7) due to their large exciton binding energy up to ~200 meV (*16*–*18*). Previously, a differential equation including mono- and bimolecular decay has been used to fit the trPL spectra of 3D lead halide perovskite (*39*, *40*). With this fitting, the proportions of radiative (bimolecular) and nonradiative (monomolecular) recombinations and the PL quantum yield can be directly obtained. Unfortunately, this model cannot fit the trPL spectra of 2D perovskite $(PEA)_2PbI_4$, as the spectra contain two distinct second-order bimolecular recombinations (see sections S6 and S7). To separately resolve the radiative and nonradiative combination rates of $(PEA)_2PbI_4$, more elaborate ultrafast spectroscopy measurement needs to be performed, which is beyond the scope of this research work. However, using a simple biexponential fitting, the average lifetime including all radiative and nonradiative components can be qualitatively analyzed. Both decay times of the biexponential decay markedly decrease with increasing pressure. At a pressure greater than 3.5 GPa, the trPL intensity largely drops, synchronizing with the sharp decline of the steady-state PL in Fig. 2A.

Pressure- and fluence-dependent PL

At each pressure, we monitored the dependence of PL intensity on excitation laser power. A typical experiment at 2.7 GPa is shown in Fig. 3A, where the PL intensity increases linearly with increasing laser power. Figure 3B shows the power-dependent intensity of all pressures. We can see that in the pressure range less than 3.5 GPa, the photon counts are high and nearly the same. A sudden drop occurs when the pressure exceeds 4 GPa. All the traces can be well fitted by $I = \alpha P_W$, where P_W is the excitation laser power and α is the intensity coefficient. α is plotted as a function of pressure in Fig. 3C (blue square). It is nearly constant at first, suggesting that the light-emitting efficiency is unmodified by pressure. However, α drops sharply when the crystal encounters a pressure range greater than 4 GPa, indicating a very poor emission efficiency.

Pressure-dependent radiative and nonradiative characteristics

The pressure-dependent average PL lifetime $\langle\tau\rangle$ is also shown in Fig. 3C (red circle), which is calculated from $\langle\tau\rangle = (A_1\tau_1 + A_2\tau_2)/(A_1 + A_2)$, where τ_1, τ_2, A_1, and A_2 are lifetime and amplitude of the two exponential components (see fig. S8 and table S1). Other than α that presents a plateau at 0 to 3.5 GPa, $\langle\tau\rangle$ monotonously decreases until the PL fully

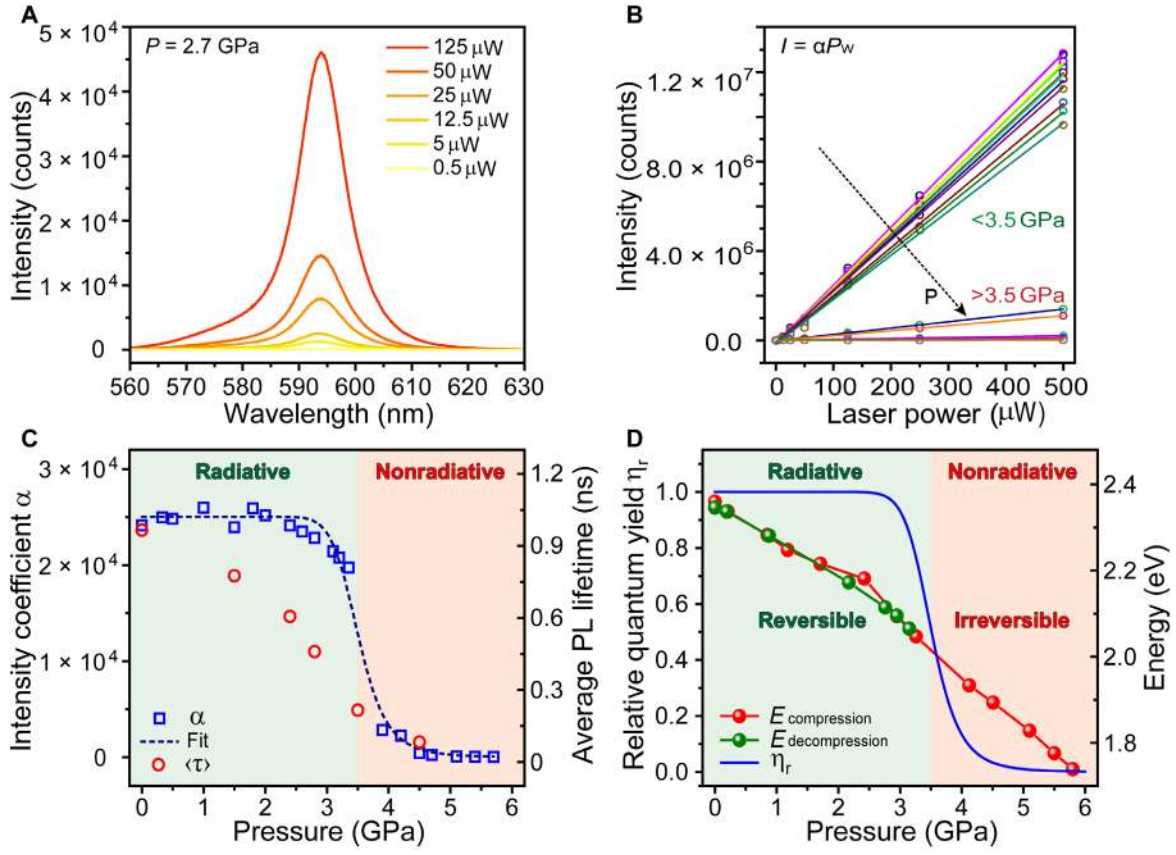

Fig. 3. Analyses and evaluation of the optical properties and performances of 2D perovskite under pressure. (**A**) A typical set of excitation power–dependent PL spectra of 2D perovskite at 2.7 GPa. (**B**) Power-law fittings of power-dependent PL intensity of 2D perovskite at all pressures; the dotted arrow points to the direction of increasing pressure. (**C**) Pressure dependence of intensity coefficient and average PL lifetime of 2D perovskite. (**D**) Evolution of PL energy position and the corresponding relative quantum yield. The green trace shows the reversibility of the PL during decompression, which only happens in optical reversible region less than 3.5 GPa.

quenches. The pressure dependence of α can be fitted (blue dash line in Fig. 3C) by the following relationship

$$\alpha = \frac{\alpha_0}{1 + ae^{-\lambda/P}} \quad (1)$$

where α_0 is the initial intensity coefficient without pressure and a and λ are fitting parameters. The relationship is a modified Arrhenius-like phenomenological model to describe the pressure-induced changes in the optical response. While $a = \tau_r/\tau_{nr}$ relates to the competition between nonradiative and radiative recombination channels at infinitely great pressure, λ, with the units of pressure, can approximately evaluate the transition from semiconductor (radiative)– to metal (nonradiative)–like behavior. By fitting α_0 versus pressure, we obtain $a = (4.37 \pm 1.12) \times 10^6$ and λ = (53.7 ± 8.2) GPa. The value of λ is in the typical pressure range where the metalization takes place for halide perovskite (*21*). Using the parameters, we can obtain the relative quantum yield of $(PEA)_2PbI_4$ (η_r) under the applied pressure. Since quantum yield η is proportional to the PL intensity coefficient α, we have the relationship between relative (η_r) and initial zero-pressure quantum yield (η_0): $\eta_r = \eta/\eta_0 = \alpha/\alpha_0$. Hence, the pressure dependence of relative quantum yield is $\eta_r = 1/(1 + ae^{-\lambda/P})$.

The plot of the relative quantum yield is shown in Fig. 3D (blue line), along with the energy evolution of PL (green and red traces) as function of pressure. The (relative) quantum yield is nearly unchanged before 3.5 GPa, but markedly drops after, following the behavior of the intensity and PL lifetimes. The optical performance of $(PEA)_2PbI_4$ with pressure is distinctly divided into highly radiative (0 to 3.5 GPa) and nonradiative (>3.5 GPa) regions. Comparing to the energy evolution of PL, we can see that the reversible and the highly radiative regions overlap. In this reversible and radiative region, η(η_r) is nearly constant but ⟨τ⟩ decreases, which indicates that the radiative recombination rate is enhanced by pressures below 3.5 GPa. That is, the material emits light even more efficiently than at 0 pressure. As a result, $(PEA)_2PbI_4$ has both wide tunability of bandgap and constant quantum yield at modest pressure range, which might be a strong implication for the use of 2D organolead halide perovskites in optoelectronics modulated by pressure.

Structural change revealed by XRD with synchrotron radiation and first-principles calculation

Generally, applying high pressure to direct bandgap semiconductors will increase the bandgap, because the binding force to the outer electrons will increase as lattice constant (interatomic distance) decreases. A strong compression usually creates limited energy changes, as distortion and phase transitions always take place. At the same time, the distortion of the lattice and the bending of chemical bonds can seriously disturb the crystal field and disorder the overlap of wave function

between atoms in compound semiconductors, making the quantum yield to drop rapidly. Similar results have been reported in traditional III-V and II-VI semiconductors (*41*, *42*) and in organolead halide perovskites (*21*, *26*, *43*).

However, 2D perovskite $(PEA)_2PbI_4$ presents large bandgap tunability with constant quantum yield under pressure, which is much more advantageous than conventional semiconductors. The result suggests that there exists a unique evolution of crystal lattice structure induced by hydrostatic pressure. These changes have been investigated by synchrotron radiation XRD under pressures from 0 to 20 GPa, as shown in Fig. 4A. The diffraction angle 2θ of XRD peaks increases with increasing pressure, which is a sign of the compression of the crystal. From 6.2 to 10.2 GPa, the XRD peaks do not shift, meaning that the compression saturates. However, after 10.2 GPa, the peaks largely broaden, indicating that the crystal lattice structure is getting disordered under high pressures. For the analysis, we focus on the pressure from 0 to 6.2 GPa, since the optical tunability sits in the range and the corresponding lattice structure changes orderly. By doing Rietveld refinement, pressure-dependent unit cell parameters can be extracted (see Materials and Methods). Figure 4B shows the unit cell volume reducing in the form of V/V_0, where V_0 is the initial volume at ambient pressure. We can see the compression saturates at 6.2 GPa, where the cell volume change is around $V/V_0 = 0.84$. The pressure dependence of the volume variation can be fitted using the so-called Birch-Murnaghan equation (*44*), which is given as

$$P(V) = \frac{3B_0}{2}\left[\left(\frac{V_0}{V}\right)^{\frac{7}{3}} - \left(\frac{V_0}{V}\right)^{\frac{5}{3}}\right]\left\{1 + \frac{3}{4}(B_0' - 4)\left[\left(\frac{V_0}{V}\right)^{\frac{2}{3}} - 1\right]\right\} \quad (2)$$

where B_0 is bulk modulus, which measures the compressibility of a material. B_0' is the derivative of B_0 with respect to pressure. Here, we assume that $B_0' = 4$, which is a common assumption when the reduction of volume has roughly a linear dependence on pressure. The bulk modulus B_0 of $(PEA)_2PbI_4$ is estimated to be 26.8 GPa. Comparing to its 3D counterparts ($MAPbI_3$ and $FAPbI_3$), which also experience similar reductions of volume (*19*, *27*, *43*), the bulk modulus of $(PEA)_2PbI_4$ is markedly greater (13.6 GPa of $MAPbI_3$ and 11.0 GPa of $FAPbI_3$). The compressibility of a material is inversely proportional to its bulk modulus. Therefore, the compressibility of $(PEA)_2PbI_4$ is much smaller than that of 3D perovskites. That is, 2D perovskite $(PEA)_2PbI_4$ is stiffer and more resistant to compression, thus experimentally showing smaller volume change with respect to pressure change.

What makes it interesting is that the above result apparently goes against the intuitive judgment on $(PEA)_2PbI_4$, which seems easier to get compressed since the long-chain ligands leave sufficient space to reduce the volume. This stiff behavior of $(PEA)_2PbI_4$ must be retraced to an unusual lattice change. XRD (Fig. 4D) and first-priciples calculation (Fig. 4E) identically show that evolution trends of lattice constants *a*, *b*, and *c* of $(PEA)_2PbI_4$ under pressure are distinctively divided into two. The deformation Δ*c* (~2 Å) is five times greater than Δ*a* (~0.39 Å) and Δ*b* (~0.47 Å). Even with the valuation of percentage, the deformation along *c* axis (6.0%) is still noticeably greater than *a* axis (4.4%) and *b* axis (5.3%), showing an average of 24% greater of decreasing under hydrostatic pressure within 6 GPa and demonstrating clear anisotropic compression. During the compression, the crystal maintains triclinic structure without any phase transition, which can be proved by the unchanged lattice angles α, β, and γ (shown in fig. S9) as well as the absence of phase transition–induced bandgap "energy jump." The *c* axis represents

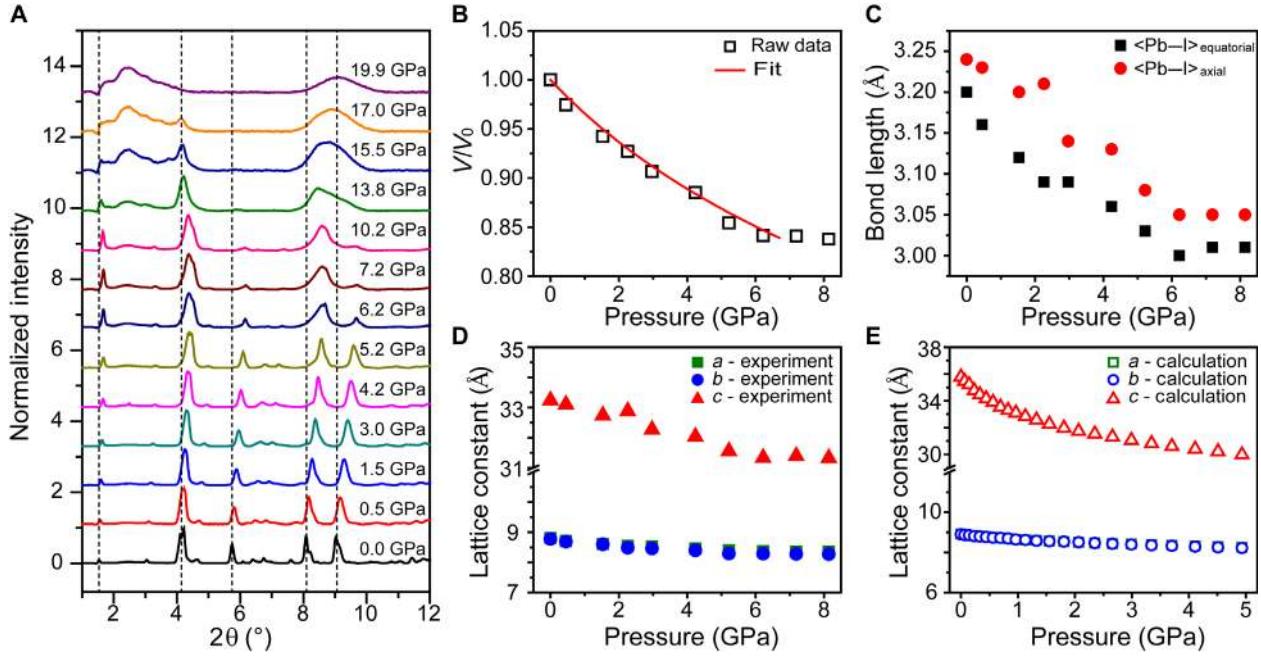

Fig. 4. Structural evolution and strongly anisotropic compression of $(PEA)_2PbI_4$ under pressure. All data are derived from XRD spectra and supported by first-principles calculation. (**A**) Synchrotron radiation XRD spectra of 2D perovskite under pressure. (**B**) Pressure dependence of unit cell volume. The volume change is represented in the form of V/V_0, in which V_0 is the initial volume at ambient pressure. The volume compression process is well fitted by Birch-Murnaghan equation. (**C**) Pressure dependence of the Pb—I bond length, which is slightly different in in-plane (<Pb—I>$_{equatorial}$) and out-of-plane (<Pb—I>$_{axial}$) directions. (**D**) Pressure dependence of unit cell parameters: *a*, *b*, and *c*. It is obvious that compression of *c* is visibly stronger than *a* and *b*, which are almost unchanged along pressure change. (**E**) Identical pressure dependence of *a*, *b*, and *c* is confirmed by first-principles calculation, which enhances the observation of anisotropic compression.

the out-of-plane direction (perpendicular to the basal plane formed by consecutive $[PbI_6]^{4-}$ octahedra), while *a* and *b* axes are in-plane directions. On the basis of the lattice constant, the length of Pb—I bond can be obtained, as shown in Fig. 4C. $<Pb—I>_{equatorial}$ and $<Pb—I>_{axial}$ are along in-plane and out-of-plane directions, which decrease equivalently (3.2 to 3.0 Å versus 3.25 to 3.05 Å). The bond length quadratic elongation and bond angle variance of Pb—I and Pb—I—Pb bond angle between adjacent octahedra are extracted from XRD data and first-principles calculation, which shows no pressure dependence (fig. S10). As a result, the compression of the unit cell is strongly anisotropic, despite the fact that hydrostatic pressure is applied from all directions. However, the compression of the $[PbI_6]^{4-}$ octahedra is fully isotropic and free of distortion and rotation. The stiff character of $(PEA)_2PbI_4$ can be attributed to its unique anisotropic deformation. Comparing to compression of 3D organolead halide perovskites in which *a*, *b*, and *c* are almost equally squeezed (*19*, *27*, *43*), the parameter *c* of $(PEA)_2PbI_4$ dominates the compression. Therefore, the volume reduction ($\Delta a \times \Delta b \times \Delta c$, Δa, and Δb are negligible) is slow, making the crystal present stiff character.

DISCUSSION

It is unexpected that hydrostatic compression of $(PEA)_2PbI_4$ is dimensionally reduced to be quasi-uniaxial. The most probable reason is that due to the 2D nature of the perovskite structure, the interlayer organic parts are much easier to deform than the inorganic layers. To verify the results, we constructed unit cell structures at 0 and 4 GPa by first-principles calculation, as shown in Fig. 5A (a video displaying the complete lattice structure evolution under pressure can be found in the Supplementary Materials). By comparing the two frames, one can hardly see noticeable changes in Pb—I inorganic counterpart (the gray and light purple spheres represent Pb and I atoms, respectively), while the organic part is greatly squeezed in the out-of-plane direction. The two paired PEA ligands, which extend from adjacent inorganic layers, are forced to move closer to each other. To reduce the volume, the carbon—carbon (C—C) bond between the benzene ring and $C_2H_4NH_3^+$ is strongly bent, making the adjacent benzene rings become parallel. The organic layers, with this self-adaptive configuration, are, to some extent, similar to buffer layers formed of springs, which are inserted between the octaheral $[PbI_6]^{4-}$ layers, as illustrated in Fig. 5B. In this simplified model, when the $(PEA)_2PbI_4$ crystal is compressed, the "spring layer" will keep shrinking and absorbing most of the compression kinetic energy; when the crystal is decompressed, the spring layer will restore and release the absorbed volume. In this manner, the pressure-induced structure changes are reversible. Moreover, the calculated structure shows that the individual $[PbI_6]^{4-}$ octahedra are geometrically preserved under pressure, which is also supported by the previous XRD and first-principles calculation results about the isotropic change of the $[PbI_6]^{4-}$ octahedral layer. No matter compression or decompression, the $[PbI_6]^{4-}$ octahedral structure will be protected and prevented from distortion and rotation. This ordered compression of $(PEA)_2PbI_4$, which protected by spring layer, is in stark contrast to 3D perovskites such as $MAPbI_3$ and $FAPbI_3$, which experience disordered compression under pressure (*20*, *21*, *26*, *27*, *43*). In 3D perovskites, the $[PbI_6]^{4-}$ frame is continuously distributed in all space; therefore, the hydrostatic pressure will act on the Pb—I bonds with the organic molecules acting as anchor points to assist the distortion and rotation of the $[PbI_6]^{4-}$ octahedra.

The unique anisotropic compression of 2D perovskite $(PEA)_2PbI_4$ causes its constant optical performance during bandgap modulation. It is well-understood that distortion and bending of chemical bonds seriously break the original crystal field and disorder the wave function overlap between atoms in semiconductors, suppressing the efficiency of band-edge transition (*21*, *41*, *42*). However, the quasi-uniaxial compression of $(PEA)_2PbI_4$ perfectly preserves the octahedral geometry of $[PbI_6]^{4-}$ and thus maintains the stability and quality of Pb—I bonds. As a result, the efficiency of band-edge transition can be maintained to the highest degree during the compression. This can also explain the optical reversible and irreversible regions, which were determined by PL spectroscopy. The reversible and radiative region is likely to be within the self-adaptive range of the organic layers. After certain pressure (>4 GPa), the organic layer inevitably reaches compression limit, the anisotropy decreases, and the octaheral $[PbI_6]^{4-}$ structure starts to distort and rotate. Under this scenario, the irreversible and nonradiative region takes place, just like what 3D perovskites experience at much lower pressure. Note that for different 2D perovskites, there could be organic ligands with different length and configuration, which can also affect the structural and electronic evolution under high pressure. Taking into account, the previous results in $[(BA)_2(MA)_{n-1}Pb_nI_{3n+1}$, $n = 1, 2, 3, 4]$ (*28*–*30*), we believe that longer ligands in $(PEA)_2PbI_4$ can help to reduce phase transition, and the benzene termination can simplify and stabilize the configuration of organic layers during compression. As a result, we do not observe any phase transition and octahedral distortion or rotation under moderate pressure range.

Figure 5D shows the projected density of states (PDOS) on atoms and the band structure of $(PEA)_2PbI_4$ at 0 and 4 GPa. The energy bandgap maintains direct at Γ point and shows a much bigger pressure-induced red shift than 3D perovskites. However, the nearly unchanged $[PbI_6]^{4-}$ size in the reversible region can hardly explain the large bandgap change, so there must be other reasons that could be related to the multiple quantum well structure. As shown in Fig. 5C, the compression of $(PEA)_2PbI_4$ can be simplified to the compression of a single type I quantum well. We know that the thickness of the organic layer decreases much faster than the $[PbI_6]^{4-}$ octahedral layer under pressure, which means that the barrier layers of the quantum well will become thinner. The thinner barrier layers will decrease the barrier potential, allowing more leakage of the electron (hole) wave function that results from the weakening of the quantum confinement effect. The bandgap change under pressure can be attributed to two main factors: $\Delta E_g(P) = \Delta E_{PbI}(P) + \Delta E_{QC}(P)$, where ΔE_{PbI} and ΔE_{QC} indicate the contributions from changes of the Pb—I bond and the quantum confinement effect, respectively. In this manner, the pressure-induced weakening of quantum confinement ($\Delta E_{QC} < 0$) will cause the bandgap red shift of $(PEA)_2PbI_4$. Using the structure and band structure parameters obtained from the XRD and first-principles calculation results, ΔE_{QC} can be calculated (calculation details can be found in section S4). Figure 5E shows the energy position of the bound states at different barrier potentials (E_1 and H_1 are in orange and cyan, respectively, and E_2 and H_2 are in gray), and the barrier potential at each pressure can be given by the PDOS on Pb, I, and C atoms, as shown in Fig. 5F [barrier potential for electron (U_e) and hole (U_h) are in orange and cyan traces, respectively]. By tracking the energy change of bound states E_1 and H_1, the pressure-dependent ΔE_{QC} can be obtained and shown as the black trace in Fig. 5F. The quantum confinement weakening becomes stronger and stronger with increasing pressure and lastly saturates at pressure around 3 to 4

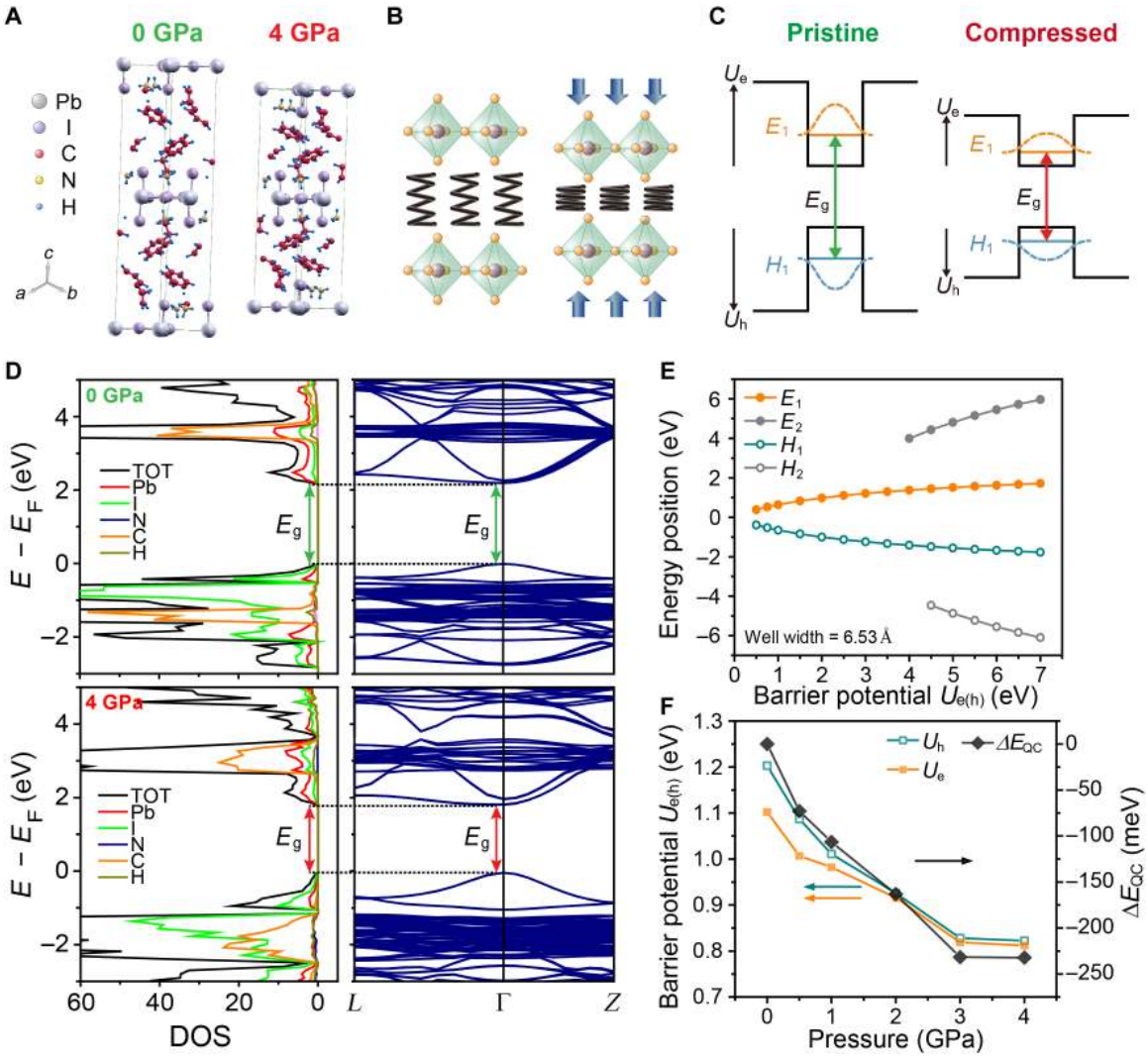

Fig. 5. Strongly anisotropic compression induced band structure change of $(PEA)_2PbI_4$. (**A**) Unit cell configuration under 0 and 4 GPa obtained from first-principles calculation. (**B**) Illustration of the compression and decompression process under hydrostatic high pressure. The springs represent the pairs of PEA molecules, which can elastically shrink and stretch, thus self-adapting to different pressures. (**C**) Schematic of a single type I quantum well with inorganic layer sandwiched by organic layers. Bound states exist in both the upper and bottom halves of the quantum well, stemming from the confinement of electrons and holes. (**D**) Projected density of states (PDOS) on each atom in $(PEA)_2PbI_4$ and the corresponding band structures at 0 and 4 GPa. The band structure diagram is shown in a particular symmetry direction along *L*-Γ-*Z* to emphasize the bandgap. The full version can be seen at fig. S3. (**E**) The energy positions of bound states as functions of barrier potential. The first and second bound states E_1 and H_1 are in orange and cyan, and E_2 and H_2 are in gray. (**F**) The pressure dependence of the barrier potential (U_e and U_h are in orange and cyan traces) and the weakening of quantum confinement (black trace).

GPa with $\Delta E_{QC} \approx -250$ meV. As a result, the weakening of quantum confinement contributes significantly (250 of 320) to the bandgap red shift in the reversible region. Note that the dielectric confinement of $(PEA)_2PbI_4$ can be modified by pressure. Since the organic barrier layer has a smaller dielectric constant (ϵ_b) than the inorganic well (ϵ_w), the electrical dipoles will be screened inside the well, and in this manner, the exciton binding energy is enhanced. Both ϵ_b and ϵ_w will change under high pressure (*45*, *46*), and thus, the dielectric confinement will change accordingly. The precise changes of the overall dielectric confinement and the contribution from each counterpart as functions of pressure are issues worth further experimental and theoretical studies.

3D perovskite can be regarded as an extreme case of 2D perovskite with zero quantum confinement effect. However, the lattice compression under pressure still gives rise to bandgap red shifts (*19*–*22*, *25*–*27*), which is opposite to the blue shift in most of the conventional semiconductors (*47*). For the irreversible region of $(PEA)_2PbI_4$, the red shift continues after the saturation of the quantum confinement weakening, which should be taken over by the compression of the $[PbI_6]^{4-}$ octahedral structure, similar to 3D perovskite. A unique feature can be seen in the PDOS diagram that the I s orbital and Pb p orbital dominate the valence band minimum (VBM) and conduction band minimum (CBM), respectively. However, In III-V or II-VI semiconductors, band extrema are swapped, meaning that p-orbital and s-orbital states occupy VBM and CBM, respectively. Because of the linear configuration of p orbital, it will be affected by the interatomic distance variation more intensely than s orbital in symmetric configuration. Applying pressure will largely increase the binding force to p-orbital electrons

and pull down its energy level from the vacuum level. For lead halide perovskite, pressure will bring down CBM (p orbital), thus narrowing the bandgap (as shown in Fig. 5C). For conventional semiconductors, VBM (p orbital) will be reduced so that the bandgap broadens. This inverse order of p-s transition can also explain the unconventional red shift of PL observed for lead halide perovskites by decreasing temperature (*8*, *33*).

In conclusion, we report an ultrabroad tunability of ~320 meV in 2D perovskite $(PEA)_2PbI_4$ by a moderate pressure ranging from 0 to 3.5 GPa. This PL red-shift turnability is fully reversible and immediately responds to pressure changes, with a quantum yield almost staying constant. Using simple modeling, it can be concluded that the excitonic recombination via radiative channel is rather enhanced within 3.5 GPa, in contrary to previous high-pressure studies in 3D organolead halide perovskites. Synchrotron radiation XRD and first-principles calculation consistently confirm that the compression process of $(PEA)_2PbI_4$ is highly anisotropic, which can be regarded as quasi-uniaxial deformation along the out-of-plane direction. This quasi-uniaxial compression primarily squeezes the organic ligands and thus avoids the distortion of Pb—I bonds. The prominent thickness reduction of the organic barrier layers releases the quantum confinement of $[PbI_6]^{4-}$ octahedral layers and therefore contributes predominantly the bandgap red shift in the reversible region. It is noticeable that the functional pressure range is relatively low and mechanically achievable without the need of DAC, which suggests the considerable potential of in situ optoelectronic applications of 2D materials or structures with pressure as a tuning knob.

MATERIALS AND METHODS

Sample preparation

Bulk crystals of $(PEA)_2PbI_4$ were synthesized by supersaturation precipitation method. Stoichiometric moles of three precursors: $C_6H_5C_2H_4NH_2$, HI, and PbI_2 were added in a round flask in γ-butyrolactone solvent until the solution became saturated. During the addition, the mixture was vigorously stirred by a magnetic stirrer in a hot oil bath to maintain clear yellow solution. After that, the round flask was allowed to evaporate slowly at 70°C in a vented oven for several days. After 3 to 7 days, orange and laminar crystals with millimeter size were collected and dried in vacuum at room temperature. After synthesis, the as-grown crystal flakes were mechanically exfoliated using scotch tape until the size and thickness matched the chamber size of the DAC. Then, the crystal microplates were transferred into the DAC using a sharp tungsten probe under stereoscopic microscope.

High pressure

A series of high-pressure experiments were performed using a symmetric DAC with a pair of 500-μm culets. A gasket was made from a 250-μm-thick T301 steel piece, by indenting to 45 μm and subsequently drilling in the center to form a hole of 150-μm diameter as the sample chamber. Monitoring pressure of the sample chamber in DAC was achieved by collecting ruby fluorescence spectra from ruby spheres loaded in the chamber (fig. S1). Silicone oil as the pressure transmission medium was compressively loaded in the sample chamber to offer a continuous hydrostatic pressure applied on the samples.

Raman scattering measurements

Raman scattering measurement was performed in backscattering geometry using a micro-Raman spectrometer (Horiba T64000). The excitation laser was introduced using a 50× long focus lens, and Raman signals were collected through the same lens. A forestage triple grating system with following grating (1800 g/mm) was used to disperse the Raman signal to achieve as low frequency as 6 cm^{-1}. To avoid in resonance with the PL of 2D perovskite, 532- and 633-nm lasers were alternatively used. When the emission was in the green to yellow range, 633 nm was used for excitation. When entering the red emission range, 532 nm was used.

PL measurements

PL spectra were taken in backscattering geometry using a micro-Raman spectrometer (Horiba HR800). A 488-nm laser (Argon ion) was introduced using a 50× long focus lens, and emission signals were collected through the same lens, resolved by a grating (300 g/mm) and imaged with a liquid nitrogen–cooled charge-coupled device (CCD) detector. A 490-nm long-wavelength pass filter was mounted in front of the CCD detector to filter out the excitation line.

TrPL measurements

The fluorescence lifetime measurement was performed using a confocal microscope with a 50× long focus lens. A 400-nm pulse excitation (8 MHz, 100 fs) was introduced to the sample, and the PL emission from sample was analyzed by a single-photon avalanche diode to resolve the time decay. A 458-nm long-pass and 720-nm short-pass filter were used to select out the PL.

Synchrotron radiation XRD

The synchrotron radiation XRD measurements under high pressure were performed at GeoSoilEnviroCARS (GSECARS), beamline 13-BM-C of the Advanced Photon Source, Argonne National Laboratory. A monochromatic x-ray beam was used with a wavelength of 0.434 Å. Experimental fitting of synchrotron radiation XRD data was carried out using TOPAS3 (*48*) in a whole powder pattern fitting approach.

First-principles calculations

Density functional theory calculations with gradient-corrected Perdew-Burke-Ernzerhof functional (*49*) were carried out using the Vienna Ab initio Simulation Package (*50*). The PAW pseudopotentials were used. We used a relatively large cutoff energy of 500 eV. The total energies were converged within 1 meV per atom. We used the atomic coordinates provided by Mitzi's group (*51*) to construct an initial structure described by a space group of $P\bar{1}$ that corresponds to a lowest-symmetry triclinic crystal system. Starting from the experimental lattice parameters of a = 8.7398 Å, b = 8.7403 Å, c = 32.9952 Å, α = 84.646°, β = 84.657°, and γ = 89.643°, with a Monkhorst-Pack k-point sampling mesh of 5 × 5 × 1, we used the constant-volume algorithm to search for the lowest-energy state. Subsequently, the volume was either increased or decreased by 3% to start a new constant-volume calculation, where the volume varied between 2815.97 and 2024.01 $Å^3$. The total energy as a function of volume was recorded, and pressure was deduced.

SUPPLEMENTARY MATERIALS

Supplementary material for this article is available at http://advances.sciencemag.org/cgi/content/full/5/7/eaav9445/DC1

Section S1. Calibration of pressure using emission line of ruby sphere
Section S2. Crystal quality and layer orientation of $(PEA)_2PbI_4$ flake
Section S3. Band structure and bandgap evolution under pressure
Section S4. Analyses of the quantum confinement effects under pressure

REFERENCES AND NOTES

1. A. Kojima, K. Teshima, Y. Shirai, T. Miyasaka, Organometal halide perovskites as visiblelight sensitizers for photovoltaic cells. *J. Am. Chem. Soc.* **131**, 6050–6051 (2009).
2. M. A. Green, A. Ho-Baillie, H. J. Snaith, The emergence of perovskite solar cells. *Nat. Photonics* **8**, 506–514 (2014).
3. M. Liu, M. B. Johnston, H. J. Snaith, Efficient planar heterojunction perovskite solar cells by vapour deposition. *Nature* **501**, 395–398 (2013).
4. H. Zhou, Q. Chen, G. Li, S. Luo, T.-b. Song, H.-S. Duan, Z. Hong, J. You, Y. Liu, Y. Yang, Interface engineering of highly efficient perovskite solar cells. *Science* **345**, 542–546 (2014).
5. Q. Zhang, S. T. Ha, X. Liu, T. C. Sum, Q. Xiong, Room-temperature near-infrared high-Q perovskite whispering-gallery planar nanolasers. *Nano Lett.* **14**, 5995–6001 (2014).
6. G. Xing, N. Mathews, S. S. Lim, N. Yantara, X. Liu, D. Sabba, M. Grätzel, S. Mhaisalkar, T. C. Sum, Low-temperature solution-processed wavelength-tunable perovskites for lasing. *Nat. Mater.* **13**, 476–480 (2014).
7. H. Zhu, Y. Fu, F. Meng, X. Wu, Z. Gong, Q. Ding, M. V. Gustafsson, M. T. Trinh, S. Jin, X.-Y. Zhu, Lead halide perovskite nanowire lasers with low lasing thresholds and high quality factors. *Nat. Mater.* **14**, 636–642 (2015).
8. J. Xing, X. F. Liu, Q. Zhang, S. T. Ha, Y. W. Yuan, C. Shen, T. C. Sum, Q. Xiong, Vapor phase synthesis of organometal halide perovskite nanowires for tunable room-temperature nanolasers. *Nano Lett.* **15**, 4571–4577 (2015).
9. D. Shi, V. Adinolfi, R. Comin, M. Yuan, E. Alarousu, A. Buin, Y. Chen, S. Hoogland, A. Rothenberger, K. Katsiev, Y. Losovyj, X. Zhang, P. A. Dowben, O. F. Mohammed, E. H. Sargent, O. M. Bakr, Low trap-state density and long carrier diffusion in organolead trihalide perovskite single crystals. *Science* **347**, 519–522 (2015).
10. S. T. Ha, X. Liu, Q. Zhang, D. Giovanni, T. C. Sum, Q. Xiong, Synthesis of organic–inorganic lead halide perovskite nanoplatelets: Towards high-performance perovskite solar cells and optoelectronic devices. *Adv. Opt. Mater.* **2**, 838–844 (2014).
11. Q. Zhang, R. Su, X. Liu, J. Xing, T. C. Sum, Q. Xiong, High-quality whispering-gallerymode lasing from cesium lead halide perovskite nanoplatelets. *Adv. Funct. Mater.* **26**, 6238–6245 (2016).
12. I. C. Smith, E. T. Hoke, D. Solis-Ibarra, M. D. McGehee, H. I. Karunadasa, A layered hybrid perovskite solar-cell absorber with enhanced moisture stability. *Angew. Chem. Int. Ed.* **126**, 11414–11417 (2014).
13. A. Mei, X. Li, L. Liu, Z. Ku, T. Liu, Y. Rong, M. Xu, M. Hu, J. Chen, Y. Yang, A holeconductor–free, fully printable mesoscopic perovskite solar cell with high stability. *Science* **345**, 295–298 (2014).
14. M. Saliba, T. Matsui, J.-Y. Seo, K. Domanski, J.-P. Correa-Baena, M. K. Nazeeruddin, S. M. Zakeeruddin, W. Tress, A. Abate, A. Hagfeldt, M. Grätzel, Cesium-containing triple cation perovskite solar cells: Improved stability, reproducibility and high efficiency. *Energ. Environ. Sci.* **9**, 1989–1997 (2016).
15. J. Xing, Y. Zhao, M. Askerka, L. N. Quan, X. Gong, W. Zhao, J. Zhao, H. Tan, G. Long, L. Gao, Z. Yang, O. Voznyy, J. Tang, Z.-h. Lu, Q. Xiong, E. H. Sargent, Color-stable highly luminescent sky-blue perovskite light-emitting diodes. *Nat. Commun.* **9**, 3541 (2018).
16. L. Dou, A. B. Wong, Y. Yu, M. Lai, N. Kornienko, S. W. Eaton, A. Fu, C. G. Bischak, J. Ma, T. Ding, N. S. Ginsberg, L.-W. Wang, A. P. Alivisatos, P. Yang, Atomically thin two-dimensional organic-inorganic hybrid perovskites. *Science* **349**, 1518–1521 (2015).
17. H. Tsai, W. Nie, J.-C. Blancon, C. C. Stoumpos, R. Asadpour, B. Harutyunyan, A. J. Neukirch, R. Verduzco, J. J. Crochet, S. Tretiak, L. Pedesseau, J. Even, M. A. Alam, G. Gupta, J. Lou, P. M. Ajayan, M. J. Bedzyk, M. G. Kanatzidis, A. D. Mohite, High-efficiency two-dimensional Ruddlesden–Popper perovskite solar cells. *Nature* **536**, 312–316 (2016).
18. J. Wang, R. Su, J. Xing, D. Bao, C. Diederichs, S. Liu, T. C. H. Liew, Z. Chen, Q. Xiong, Room temperature coherently coupled exciton polaritons in two-dimensional organic-inorganic perovskite. *ACS Nano* **12**, 8382–8389 (2018).
19. F. Capitani, C. Marini, S. Caramazza, P. Postorino, G. Garbarino, M. Hanfland, A. Pisanu, P. Quadrelli, L. Malavasi, High-pressure behavior of methylammonium lead iodide ($MAPbI_3$) hybrid perovskite. *J. Appl. Phys.* **119**, 185901 (2016).
20. L. Kong, G. Liu, J. Gong, Q. Hu, R. D. Schaller, P. Dera, D. Zhang, Z. Liu, W. Yang, K. Zhu, Y. Tang, C. Wang, S.-H. Wei, T. Xu, H.-k. Mao, Simultaneous band-gap narrowing and carrier-lifetime prolongation of organic–inorganic trihalide perovskites. *Proc. Natl. Acad. Sci. U.S.A.* **113**, 8910–8915 (2016).
21. A. Jaffe, Y. Lin, W. L. Mao, H. I. Karunadasa, Pressure-induced metallization of the halide perovskite $(CH_3NH_3)PbI_3$. *J. Am. Chem. Soc.* **139**, 4330–4333 (2017).
22. M. Szafrański, A. Katrusiak, Mechanism of pressure-induced phase transitions, amorphization, and absorption-edge shift in photovoltaic methylammonium lead iodide. *J. Phys. Chem. Lett.* **7**, 3458–3466 (2016).
23. G. Xiao, Y. Cao, G. Qi, L. Wang, C. Liu, Z. Ma, X. Yang, Y. Sui, W. Zheng, B. Zou, Pressure effects on structure and optical properties in cesium lead bromide perovskite nanocrystals. *J. Am. Chem. Soc.* **139**, 10087–10094 (2017).
24. Y. Nagaoka, K. Hills-Kimball, R. Tan, R. Li, Z. Wang, O. Chen, Nanocube superlattices of cesium lead bromide perovskites and pressure-induced phase transformations at atomic and mesoscale levels. *Adv. Mater.* **29**, 1606666 (2017).
25. H. Zhu, T. Cai, M. Que, J.-P. Song, B. M. Rubenstein, Z. Wang, O. Chen, Pressure-induced phase transformation and band-gap engineering of formamidinium lead iodide perovskite nanocrystals. *J. Phys. Chem. Lett.* **9**, 4199–4205 (2018).
26. L. Wang, K. Wang, B. Zou, Pressure-induced structural and optical properties of organometal halide perovskite-based formamidinium lead bromide. *J. Phys. Chem. Lett.* **7**, 2556–2562 (2016).
27. G. Liu, L. Kong, J. Gong, W. Yang, H.-k. Mao, Q. Hu, Z. Liu, R. D. Schaller, D. Zhang, T. Xu, Pressure-induced bandgap optimization in lead-based perovskites with prolonged carrier lifetime and ambient retainability. *Adv. Funct. Mater.* **27**, 1604208 (2017).
28. G. Liu, L. Kong, P. Guo, C. C. Stoumpos, Q. Hu, Z. Liu, Z. Cai, D. J. Gosztola, H.-k. Mao, M. G. Kanatzidis, R. D. Schaller, Two regimes of bandgap red shift and partial ambient retention in pressure-treated two-dimensional perovskites. *ACS Energy Lett.* **2**, 2518–2524 (2017).
29. G. Liu, J. Gong, L. Kong, R. D. Schaller, Q. Hu, Z. Liu, S. Yan, W. Yang, C. C. Stoumpos, M. G. Kanatzidis, H.-k. Mao, T. Xu, Isothermal pressure-derived metastable states in 2D hybrid perovskites showing enduring bandgap narrowing. *Proc. Natl. Acad. Sci. U.S.A.* **115**, 8076–8081 (2018).
30. G. Feng, Y. Qin, C. Ran, L. Ji, L. Dong, W. Li, Structural evolution and photoluminescence properties of a 2D hybrid perovskite under pressure. *APL Mater.* **6**, 114201 (2018).
31. H. K. Mao, J.-A. Xu, P. M. Bell, Calibration of the ruby pressure gauge to 800 kbar under quasihydrostatic conditions. *J. Geophys. Res.* **91**, 4673–4676 (1986).
32. S. Rekhi, L. S. Dubrovinsky, S. K. Saxena, Temperature-induced ruby fluorescence shifts up to a pressure of 15GPa in an externally heated diamond anvil cell. *High Temp. High Press.* **31**, 299–305 (1999).
33. M. I. Dar, G. Jacopin, S. Meloni, A. Mattoni, N. Arora, A. Boziki, S. M. Zakeeruddin, U. Rothlisberger, M. Grätzel, Origin of unusual bandgap shift and dual emission in organicinorganic lead halide perovskites. *Sci. Adv.* **2**, e1601156 (2016).
34. D. B. Straus, S. Hurtado Parra, N. Iotov, J. Gebhardt, A. M. Rappe, J. E. Subotnik, J. M. Kikkawa, C. R. Kagan, Direct observation of electron–phonon coupling and slow vibrational relaxation in organic–inorganic hybrid perovskites. *J. Am. Chem. Soc.* **138**, 13798–13801 (2016).
35. T. T. H. Do, A. G. del Águila, C. Cui, J. Xing, Z. Ning, Q. Xiong, Optical study on intrinsic exciton states in high-quality $CH_3NH_3PbBr_3$ single crystals. *Phys. Rev. B* **96**, 075308 (2017).
36. R. Claus, H. H. Hacker, H. W. Schrötter, J. Brandmüller, S. Haussühl, Low-frequency opticalphonon spectrum of benzil. *Phys. Rev.* **187**, 1128 (1969).
37. Z. Q. Ren, L. E. McNeil, S. Liu, C. Kloc, Molecular motion and mobility in an organic single crystal: Raman study and model. *Phys. Rev. B* **80**, 245211 (2009).
38. H. Ye, G. Liu, S. Liu, D. Casanova, X. Ye, X. Tao, Q. Zhang, Q. Xiong, Molecular-barrierenhanced aromatic fluorophores in cocrystals with unity quantum efficiency. *Angew. Chem. Int. Ed.* **57**, 1928–1932 (2018).
39. T. Wang, B. Daiber, J. M. Frost, S. A. Mann, E. C. Garnett, A. Walsh, B. Ehrler, Indirect to direct bandgap transition in methylammonium lead halide perovskite. *Energ. Environ. Sci.* **10**, 509–515 (2017).
40. G. Xing, B. Wu, X. Wu, M. Li, B. Du, Q. Wei, J. Guo, E. K. Yeow, T. C. Sum, W. Huang, Transcending the slow bimolecular recombination in lead-halide perovskites for electroluminescence. *Nat. Commun.* **8**, 14558 (2017).
41. P. Y. Yu, B. Welber, High pressure photoluminescence and resonant raman study of GaAs. *Solid State Commun.* **25**, 209–211 (1978).

42. A. Mujica, A. Rubio, A. Muñoz, R. J. Needs, High-pressure phases of group-IV, III–V, and II–VI compounds. *Rev. Mod. Phys.* **75**, 863 (2003).
43. T. Ou, J. Yan, C. Xiao, W. Shen, C. Liu, X. Liu, Y. Han, Y. Ma, C. Gao, Visible light response, electrical transport, and amorphization in compressed organolead iodine perovskites. *Nanoscale* **8**, 11426–11431 (2016).
44. F. Birch, Finite elastic strain of cubic crystals. *Phys. Rev.* **71**, 809 (1947).
45. D. W. Brazier, G. R. Freeman, The effects of pressure on the density, dielectric constant, and viscosity of several hydrocarbons and other organic liquids. *Can. J. Chem.* **47**, 893–899 (1969).
46. X. Hong, T. Ishihara, A. V. Nurmikko, Dielectric confinement effect on excitons in PbI_4-based layered semiconductors. *Phys. Rev. B* **45**, 6961(R) (1992).
47. S.-H. Wei, A. Zunger, Predicted band-gap pressure coefficients of all diamond and zincblende semiconductors: Chemical trends. *Phys. Rev. B* **60**, 5404 (1999).
48. Bruker AXS Inc., TOPAS, version 3 (2005).
49. J. P. Perdew, K. Burke, M. Ernzerhof, Generalized gradient approximation made simple. *Phys. Rev. Lett.* **77**, 3865 (1996).
50. G. Kresse, J. Furthmüller, Efficient iterative schemes for ab initio total-energy calculations using a plane-wave basis set. *Phys. Rev. B* **54**, 11169 (1996).
51. K.-z. Du, Q. Tu, X. Zhang, Q. Han, J. Liu, S. Zauscher, D. B. Mitzi, Two-dimensional lead (II) halide-based hybrid perovskites templated by acene alkylamines: Crystal structures, optical properties, and piezoelectricity. *Inorg. Chem.* **56**, 9291–9302 (2017).

Acknowledgments: We thank B. Yan and D. Zhang for assistance with the synchrotron XRD measurements. The XRD experiment was performed at the 13-BM-C experimental station of the GSECARS facility at the APS. **Funding:** Q.X. acknowledges the strong support from Singapore Ministry of Education via Tier 2 grant (MOE2015-T2-1-047) and Tier 1 grants (RG 113/16 and RG 194/17). S.S. acknowledges support from National Natural Science Foundation of China (nos. 11504267 and 11604243), the Natural Science Foundation of Tianjin (no. 16JCQNJC01600), and Tianjin Municipal Education Commission Scientific Research project (2018KJ151). C.K.G. thanks the National Supercomputing Center (NSCC), Singapore and A*STAR Computational Resource Center (ACRC), Singapore for computing resources. A.G.d.Á. acknowledges the financial support of the Presidential Postdoctoral Fellowship program of the Nanyang Technological University. 13-BM-C operation is supported by COMPRES through the Partnership for Extreme Crystallography (PX^2) project, under NSF cooperative agreement EAR 11-57758. **Author contributions:** S.L., S.S., and Q.X. conceived the idea and designed the research. S.L. and S.S. performed the high-pressure setup and optical measurements. J.X. prepared the sample. C.K.G. carried out the first-principles calculation. S.S. did the synchrotron radiation XRD measurement. Y.F. and T.J.W. did the XRD refinement and structural analysis. S.L., S.S., A.G.d.Á., H.L., W.H., and Q.X. analyzed the data. A.G.d.Á. and T.T.H.D. intensively discussed on the data and manuscript. S.L., S.S., and Q.X. wrote the manuscript. All authors discussed and commented on the manuscript. S.L. and S.S. contributed equally to this work. **Competing interests:** The authors declare that they have no competing interests. **Data and materials availability:** All data needed to evaluate the conclusions in the paper are present in the paper and/or the Supplementary Materials. Additional data related to this paper may be requested from the authors.

Submitted 6 November 2018
Accepted 20 June 2019
Published 26 July 2019
10.1126/sciadv.aav9445

Citation: S. Liu, S. Sun, C. K. Gan, A. G. del Águila, Y. Fang, J. Xing, T. T. H. Do, T. J. White, H. Li, W. Huang, Q. Xiong, Manipulating efficient light emission in two-dimensional perovskite crystals by pressure-induced anisotropic deformation. *Sci. Adv.* **5**, eaav9445 (2019).